Aerodynamic fiber deposition: additive manufacturing continuous fiber reinforcement with patternable alignment

Luochang Wang, Simeng Wu, Paulson Varghese, Jung-Kun Lee, Qihan Liu*

Department of Mechanical Engineering and Materials Science, University of Pittsburgh, Pittsburgh 15213, USA

Abstract

Fiber-reinforced composites (FRC) are high-performance materials whose manufacture is constrained by the difficulty of arranging continuous fibers into complex, spatially varying orientations. This work reports aerodynamic fiber deposition (AFD), a new additive manufacturing technique that uses electrospinning to generate continuous airborne nano/microfibers and a tangent airflow to align them on a conductive target. An insulating mask on the target can localize the aligned deposition and produce fibrous layers with patternable fiber orientation by scanning the localized deposition window over the target. The deposited polymer fibers can then be pyrolyzed into inorganic fibers, which can be infiltrated with resin to produce high-performance FRC.

Keywords: aerodynamic fiber deposition; additive manufacturing; fiber reinforced composite; electrospinning; silicon carbide

1. Introduction

Fiber-reinforced composites (FRC) are lightweight high-performance materials important to various industrial sectors [1]. The manufacturing of FRC has been limited by the complexity of laying up fibers into desired orientations. High-throughput techniques such as pultrusion and filament winding are limited to objects of translational and rotational symmetry respectively, offering limited control over fiber arrangements [2]. Consequently, hand lay-up remains the most common technique for irregular geometries with non-uniform fiber arrangements despite its low throughput and susceptibility to human error [3]. Various additive manufacturing techniques have been developed to address the challenge of simultaneously achieving complex fiber arrangements and complex part geometry with limited success. FRC with chopped fibers is readily compatible with existing extrusion-based and vat photopolymerization technologies [4]. However, the performance of such composites is inferior to that of continuous fiber reinforcement. Automated fiber placement (AFP) and automated tape layup (ATL) use complex robotic setups to wrap fiber tows or tapes over curved geometries [5, 6]. However, these techniques are limited to large objects with smooth surfaces and cannot replace hand lay-up for small objects and highly curved surfaces. The high upfront cost of the robotic system also greatly limits their adoption. In contrast, extruding continuous fibers in fused deposition modeling (FDM) can produce small FRC parts at a much lower upfront cost [4]. However, the pores between filaments greatly limit the performance. Moreover, in both AFP/ATL and FDM-based FRC manufacturing, the fiber orientation is coupled to the toolpath, making it difficult to generate a space-filling toolpath while independently controlling fiber orientation.

This work develops a new technique called aerodynamic fiber deposition (AFD) for the additive manufacturing of FRC. AFD uses established fiber-spinning platforms, such as electrospinning and melt blowing [7, 8], to generate continuous airborne nano/microfibers, and then uses airflow to align them. By scanning the deposition region over a target surface, fibrous material with patternable fiber orientations can be manufactured. The fibers can then be infiltrated with a matrix to form FRC. Compared to existing robotic setups (AFP/ATL), AFD has a much lower upfront cost and is more flexible for small parts. Compared to existing FDM-based FRC printing, AFD does not generate artificial pores in the fiber deposition. Moreover, the fiber

orientation of AFD is determined by airflow independent of the toolpath, making toolpath planning much easier.

2. Aligning airborne fibers by tangent airflow

Well-established high-throughput nano/microfiber manufacturing techniques, such as electrospinning and melt blowing [7, 8], typically produce random fiber deposition. Aligned fiber deposition is commonly achieved by collecting fibers on a fast-moving target, such as rotating cylinders and conveying belts, typically with 10-100 m/s surface velocity [9-12]. However, such target speeds are impractical for additive manufacturing, which typically translates the printhead or print bed at ~1 cm/s, three to four orders of magnitude slower. Without moving the target, it is possible to align electrospun fibers using special electrode arrangements [13-15]. However, fibers are then directly deposited on the electrodes, making it impossible to pattern fiber orientations on a separate target.

The classical approach of aligning fibers using the target motion can be interpreted through the following model. Decompose the local velocity of fibers in the direction perpendicular and parallel to the target as $v_\perp$ and $v_\parallel$ (Fig. 1A). Denote the angle between the local fiber velocity and the target surface as θ. Assume the target moves in its own plane with a velocity v_{tar}. The fiber orientation in the air and $v_\parallel$ are highly random due to the bending instability in electrospinning and turbulent airflow in melt blowing [16, 17]. $v_\perp > 0$ as the fibers are carried toward the target by electric field (electrospinning) or airflow (melt blowing). During a short time τ, a fiber of length $v_\perp \tau / \sin\theta$ is deposited over the target with a relative shift of $(v_{tar} + v_\parallel)\tau$. If $v_{tar} + v_\parallel \ll v_\perp/\sin\theta$, the shift of the deposition location is negligible during the time τ. Then the random fiber orientation in the air is directly transferred to the target. When $v_{tar} + v_\parallel > v_\perp/\sin\theta$, the relative shift during the time τ is more than the length of the deposited fiber. The fiber is pulled by this shift and aligned in the direction of $v_{tar} + v_\parallel$. Since $v_\parallel$ and $v_\perp/\sin\theta$ are both random, one needs $v_{tar} \gg \langle v_\parallel \rangle + \langle v_\perp/\sin\theta \rangle$ to suppress both sources of randomness and ensure good alignment in the direction of v_{tar}. Here the angle brackets denote averaging. Since there is always some chance that θ is close to 0° (i.e., the fiber is nearly parallel to the target when deposited), there is always a fraction of fibers that cannot be aligned. The higher the v_{tar}, the larger the fraction that are aligned. This prediction agrees with qualitative observations reported in the literature [11, 12].

This work proposes to align fibers with an airflow tangent to the target with velocity v_{air} (Fig. 1B) instead of the target motion. Because micro/nanofibers are light and have a large specific surface area, they can be assumed to passively follow the airflow. Then the total relative shift during the period of τ is $(v_{tar} + v_{air} + v_\parallel)\tau$. If a sufficiently large v_{air} is applied, fibers can be aligned without v_{tar}. If $v_{tar} \ll v_{air}$, the target can be moved arbitrarily without affecting fiber alignment. We call this technique aerodynamic fiber deposition (AFD).

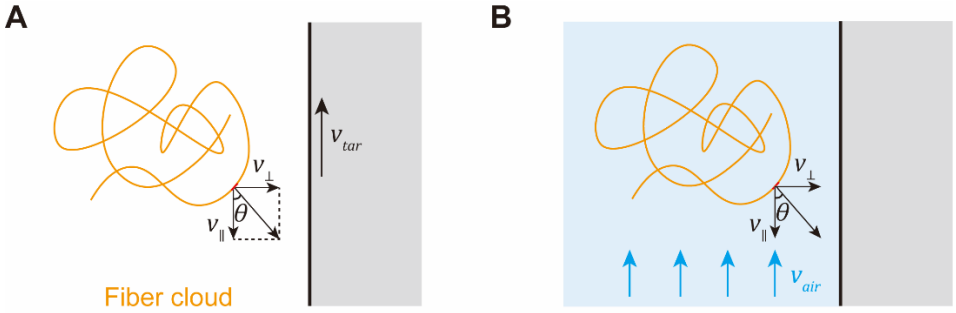

Figure 1. **(A)** How existing studies use a moving target of velocity v_{tar} to align fibers. **(B)** How aerodynamic fiber deposition (AFD) uses an airflow of v_{air} to align fibers.

We first demonstrate AFD using an electrospinning setup (Fig. 2A). We spun a 10 wt.% polyethylene oxide (PEO) aqueous solution onto a 20 cm × 30 cm conductive target. The target

is much larger than the natural deposition region (≈10 cm) so that its exact dimensions do not affect the deposition. The target is fixed, i.e., $v_{tar} = 0$. An airflow tangent to the target is applied through a flat nozzle. The airflow speed v_{air} measured at various locations near the target is marked on a photo of fiber deposition (Fig. 2B). Outside the air jet (marked by green dashed lines), $v_{air} \approx 0$; the deposited fibers are randomly oriented and spread over a circular region (marked by white dashed lines), as in conventional electrospinning [18]. The nozzle itself is made of plastic; static charge accumulating on its insulating surface repels the incoming fibers and prevents deposition onto the nozzle. Near the nozzle, the airflow has a thickness comparable to the nozzle thickness (~1 mm). Denoting this thickness as l, then it takes a time of $l/v_{\perp}$ for the fibers to go through the airflow and reach the target. By the time a fiber reaches the target, it is blown downstream by a distance of $v_{air} l \,/\, v_{\perp}$. Consequently, no fiber deposition is observed near the nozzle. Since the airflow is not perfectly uniform, the boundary of the blank region fluctuates across the width of deposition. Beyond this blank region, fibers reach the target with a high v_{air} that aligns them. Around this initial deposition site, it was found that $v_{air} \approx 20\mathrm{m/s}$ is needed to achieve good alignment (Fig. S1). Further downstream, v_{air} drops yet the fiber alignment persists. This is because the electrospun fibers are continuous: once a segment is deposited on the target, the rest of the fibers are aligned in the airflow like a flag aligned in the wind, and a high v_{air} is unnecessary. The principle of AFD is independent of the electric field and can therefore be applied to other spinning processes such as melt blowing (Fig. S2). A similar effect was also observed in rotary jet spinning [19].

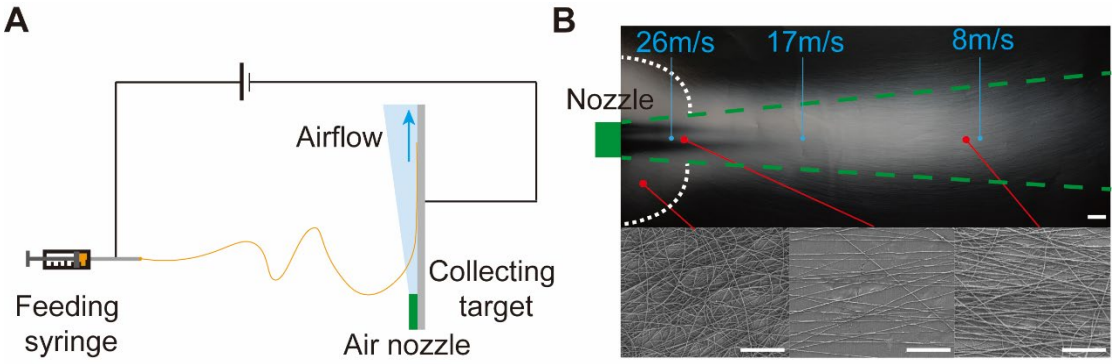

Figure 2. (A) The setup of electrospinning AFD. **(B)** Photo of the deposition produced by electrospun AFD with a scale bar of 1 cm. The bottom row shows scanning electron microscope (SEM) images of the fibers from different locations with scale bars of 10 μm.

3. Controlling deposition region by insulating masks

To achieve patternable fiber orientation, the aligned fibers must be localized to a small deposition region. Using insulating masks that prevent fiber deposition through charge accumulation is a common technique to pattern electrospun fibers [20-25]. In this work, this technique is combined with airflow to achieve localized and aligned deposition.

A mask is first used to limit deposition into a 1-cm-wide, 8-cm-long window starting from the air nozzle (Fig. 3A). The mask perfectly confines the fiber deposition in the width direction. Some fibers spill over the downstream edge, but most fibers are focused into the deposition window. SEM images show that the fiber alignment is as good as the case without the mask. Next, we try to eliminate the initial non-uniform blank region by shortening the window by 5 cm in the upstream direction (Fig. 3B). However, the deposition region does not match the window geometry. There is a short blank region near the upstream edge, similar to the blank region near the insulating nozzle. Moreover, the fiber alignment is worse although the same spinning condition is kept. When the upstream portion of the insulating mask (resistivity $5.0 \times 10^{11}\Omega \cdot \mathrm{m}$) is replaced with a guiding strip of static dissipative plastic (resistivity $2.5 \times 10^{3}\Omega \cdot \mathrm{m}$), fiber deposition is found to perfectly match the window geometry with little

fiber deposited on the guiding strip (Fig. 3C). The fiber alignment also improves, although it is not fully recovered to the level of Fig. 3A.

The difference between these three cases is interpreted through the following simulation. The air between the spinning needle and the deposition target is represented as a conductive medium where the fibers are the charge carriers (Fig. S3). The conductive target is represented by a constant electric potential boundary condition, and the insulating mask is represented by a no-current boundary condition. Instead of explicitly modeling the fibers, the conductivity of the medium is assumed to be linearly proportional to the local electric field strength, which qualitatively represents that regions of higher electric field have more fibers and more fibers lead to higher conductivity. This assumption has been verified not to affect the qualitative conclusion of the simulation (Fig. S4). The electric field is visualized on the plane going through the center of the spinning needle and the deposition window (Fig. S3). It is found that the edge between conductor and air or insulator causes field concentration (Fig. 3D). Reducing the window size on all sides significantly increases the electric field inside the deposition window (Fig. 3E). The strong electric field near the target leads to a high $v_{\perp}$, which explains the poorer fiber alignment observed in Fig. 3B. When a dissipative plastic film is used to replace the upstream part of the mask, the strong electric field can be mitigated (Fig. 3F), allowing fiber alignment to be recovered in Fig. 3C. The simulations show that the dissipative guiding strip effectively modifies the electric field when its conductance is comparable to that from the needle to the target (Fig. S5).

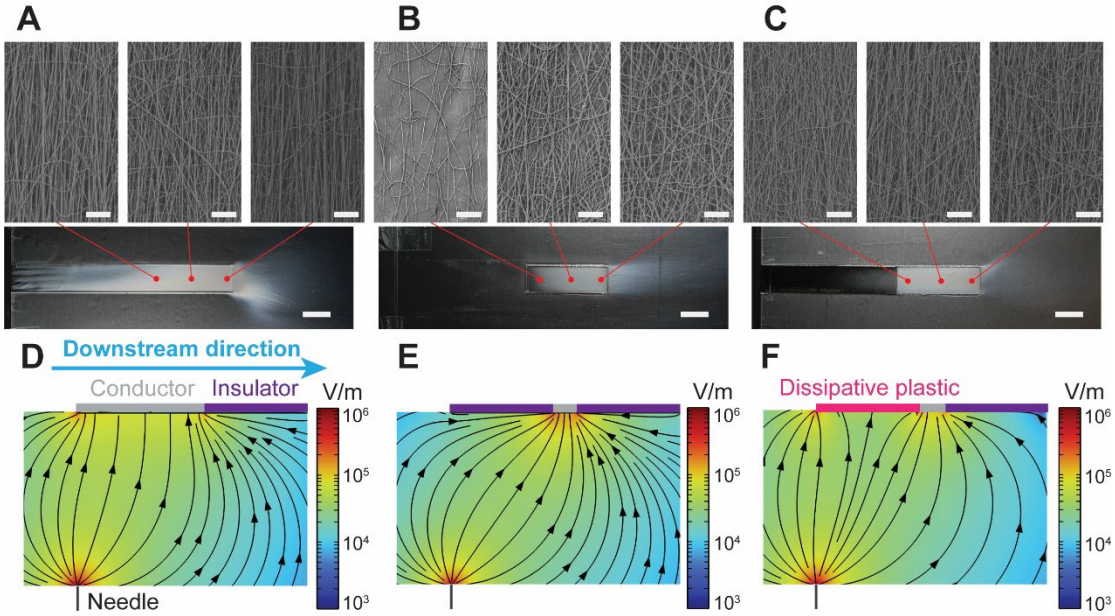

Figure 3. (A) Photo (bottom) and SEM images (top row) of the deposition using an insulating mask to limit the deposition region. **(B)** Extending the insulating mask upstream leads to a blank region near the upstream edge. The small window area leads to poor fiber alignment. **(C)** Replacing the upstream portion of the mask with a static dissipative plastic removes the blank region and recovers fiber alignment. **(D-F)** The electric field between the needle and the center of the deposition window corresponding to (A-C).

4. Patterning fiber alignment by moving targets

With control over both the fiber location and fiber alignment, AFD can pattern fiber orientation by scanning the deposition region across a target surface. This capability is demonstrated by depositing onto a conductive target through a 1 cm × 1 cm window in an insulating mask (Fig. 4A). A 1 cm × 5 cm dissipative guiding strip is placed tilted about 15° from the window. When the target is translated behind the paper window, a line of aligned fibers is deposited (Fig. 4B). Since the target translation speed v_{tar} (~5 mm/s) is much less than the airflow speed v_{air} (~10

m/s), v_{tar} cannot affect fiber alignment. Whether the target is moved in parallel or perpendicular to the airflow direction, fibers are always aligned in the direction of airflow. By depositing lines side-by-side, a continuous fiber layer of spatially varying fiber orientation can be formed.

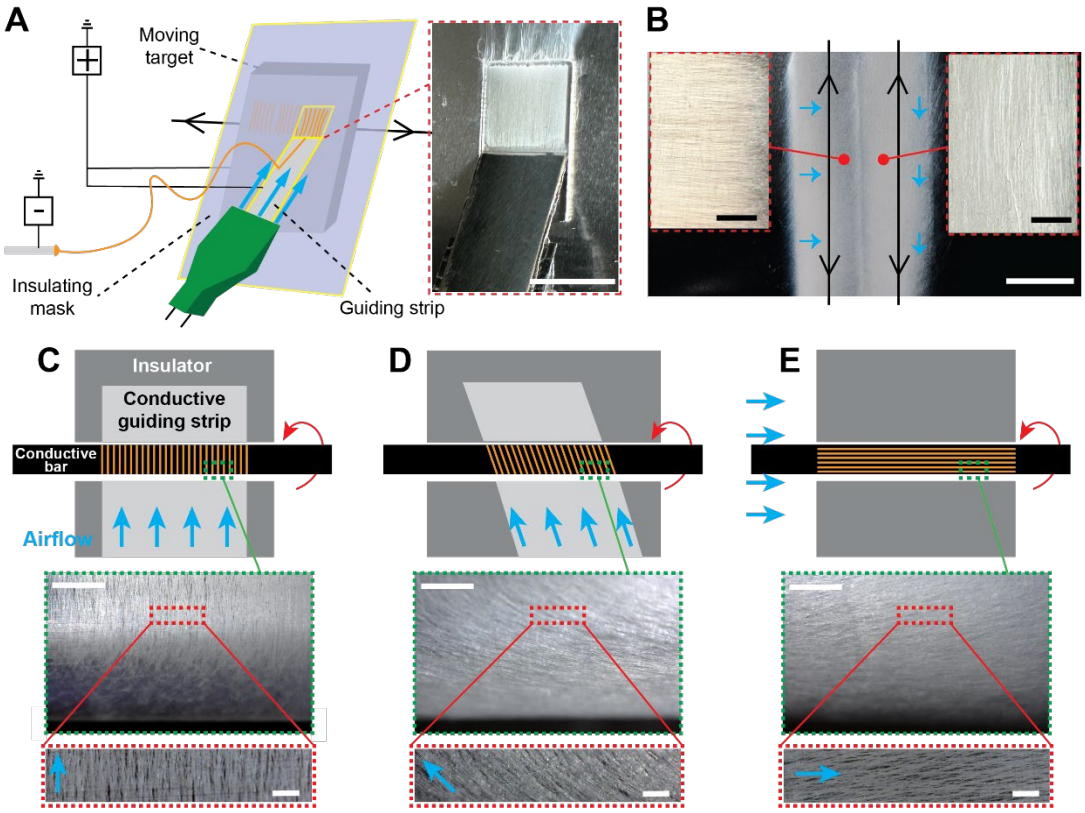

Figure 4. (A) The AFD setup to print fibrous material with patternable fiber orientation. Scale bar is 1 cm. **(B)** Fiber orientation is determined by airflow direction (blue arrows) independent of target moving direction (black arrows). A continuous layer of fibrous material with spatially varying fiber orientation can be manufactured by depositing line by line. The scale bars are 1 cm and 2 mm for the zoomed-out and zoomed-in photo respectively. **(C)** Setup using a guiding strip with a slit to deposit circumferentially aligned fibers over a bar. **(D)** Tilting the guiding plate and the airflow results in helically aligned fibers. **(E)** Longitudinally aligned fibers can be achieved with airflow alone. In (C-E), the scale bars are 1 mm for the zoom-out views (top) and 100 μm for the zoom-in views (bottom).

The same strategy can be applied to non-flat surfaces. A 12-mm-diameter metal bar is fitted through a slit in a 5 cm × 15 cm guiding strip. An airflow aligns fibers over both the guiding strip and the cylinder as the cylinder rotates at 400 rpm. The surface speed of the cylinder is $v_{tar} \approx 0.2\ \mathrm{m/s}$, much lower than the airflow speed $v_{air} \approx 20\ \mathrm{m/s}$. Consequently, fiber alignment is not affected by the cylinder rotation. By changing the direction of the airflow and the orientation of the guiding strip, circumferential (Fig. 4C), helical (Fig. 4D), and longitudinal (Fig. 4E) fiber alignment can be achieved.

5. Converting polymer fibers to inorganic fibers

Electrospinning can only directly produce polymer fibers that are either soluble in a solvent or meltable. In contrast, fiber-reinforced composites often require inorganic fibers such as glass fibers, carbon fibers, and silicon carbide (SiC) fibers [26]. This work shows that electrospun fibers can be pyrolyzed after AFD to yield inorganic fibrous structures. Such structures can then be infiltrated with matrix resin through techniques such as vacuum-assisted resin transfer

molding [27]. The process is demonstrated here with SiC fibers while the polymer-derived approach is generally applicable to a wide range of inorganic material systems [28, 29].

Polymer-derived SiC fiber synthesis starts with polycarbosilane precursors, followed by spinning, crosslinking, and pyrolysis. A commercially available allylhydridopolycarbosilane (AHPCS) precursor (SMP-730, Starfire Systems) is employed and converted into ceramic fibers through the sequence illustrated in Fig. 5A. This manufacturing procedure is combined with the AFD setup illustrated in Fig. 4C to spin a circumferentially aligned AHPCS fibrous tube of 1.2 mm thickness after 30 min of deposition (Fig. 5B). After pyrolysis, the fibrous tube shrinks isotropically by ~35% as the polymer is converted into the denser SiC (Fig. 5C and D). X-ray diffraction (XRD) confirms the formation of β-SiC phases (Fig. 5E). This fiber structure can support itself and can be infiltrated with a matrix resin following conventional FRC manufacturing practices.

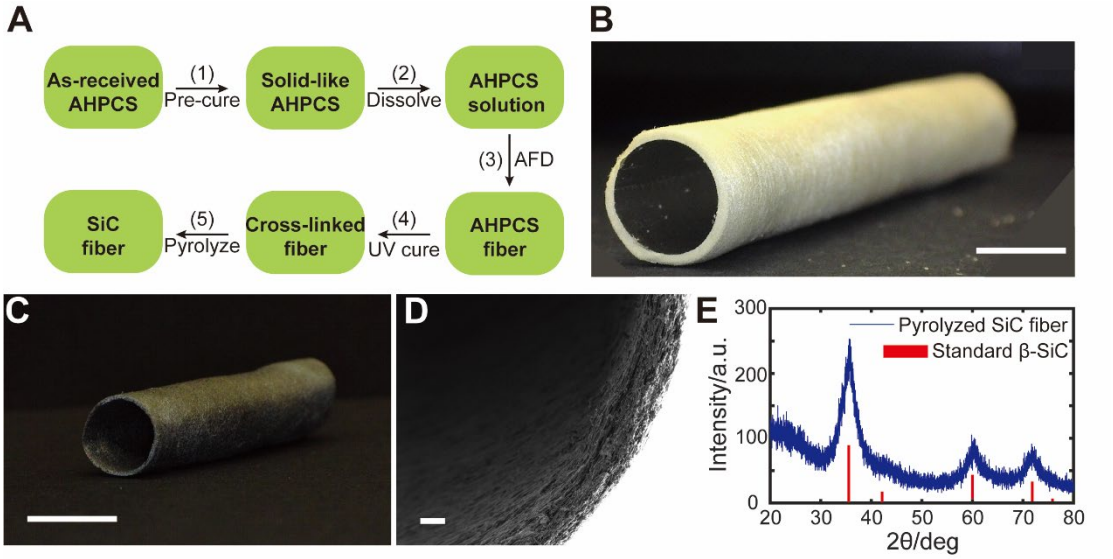

Figure 5. (A) The synthesis procedure for AFD-based SiC fibers. **(B)** AHPCS fiber tube. Scale bar is 1 cm. **(C)** The pyrolyzed SiC fiber tube. Scale bar is 1 cm. **(D)** The SEM image of the edge of the pyrolyzed SiC fiber tube. Scale bar is 100 μm. **(E)** XRD confirms the formation of β-SiC.

6. Conclusion

This work has developed aerodynamic fiber deposition (AFD), a new additive-manufacturing technique that can be used to produce continuous-fiber-reinforced composites with patternable fiber orientation. By applying a tangent airflow over a deposition window bounded by an insulating mask, AFD decouples fiber alignment from target motion: fibers are aligned by the airflow itself, so the target can be translated at the slow speeds compatible with additive manufacturing (~1 cm/s) while still yielding well-aligned deposition. By scanning the deposition window over a target and tuning the airflow direction, path orientation and fiber orientation can be independently controlled on a target surface, including non-flat surfaces. It is further shown that AFD-made polymer fibers can be converted into inorganic fibers through polymer-derived ceramic chemistry, using AHPCS-derived SiC tubes as an example.

Compared with existing continuous-fiber additive manufacturing, AFD combines the low upfront cost and small-part flexibility of FDM-based approaches with pore-free uniform fiber distribution closer to that of AFP/ATL, while avoiding the toolpath-orientation coupling of both. Together with the demonstrated route to inorganic fibers, these features position AFD as a versatile platform for the additive manufacturing of fiber-reinforced composites with tailored, spatially varying fiber orientations.

Acknowledgements
This work is supported by the National Science Foundation under Grant No. 2405116 and the Department of Energy under Grant No. DE-NE0009412.

Data availability
All data supporting the findings of this study are available within the article and its Supplementary Information.

Methods
1. AFD setup for electrospinning
The electrospun AFD setup consists of a conventional electrospinning spinneret perpendicular to a conductive target and a flat nozzle (41 mm outlet width, E-outstanding) tangent to the target. It was found that slightly tilting the target (±15°) does not noticeably affect spinning or deposition. A total voltage of 13.5 kV is applied across a 15 cm needle-to-target distance, with the needle (stainless steel) biased at +5 kV and the target at −8.5 kV. The voltage is supplied by high-voltage power supplies (ES30-20W and ES30N-20W/PRG, Gamma High Voltage Research). The split-voltage configuration is used to reduce electrostatic attraction between the fibers and surrounding objects, thereby achieving more stable spinning. The nozzle is at the same height as the spinning needle so that fibers naturally enter the airflow upstream and deposit downstream. The air velocity is tuned by adjusting a pressure regulator (PPR2-N02BG-2, PneumaticPlus) in a compressed-air line and is measured using a hot-wire anemometer (TMA-21HW, Amprobe). The spinneret is made of a 21G needle connected to a 10 ml plastic syringe mounted on a syringe pump (Fusion 200X, Chemyx).

The insulating mask is made of polycarbonate with 0.5 mm thickness (resistivity $5.0 \times 10^{11}\ \Omega \cdot m$). The static-dissipative plastic is a poly(vinyl chloride) matrix filled with a conductive carbon mesh to dissipate charge (resistivity $2.5 \times 10^{3}\ \Omega \cdot m$; McMaster-Carr 8714K67). It is bonded to aluminum foil or 304 stainless steel sheets with double-sided conductive carbon tape (Ted Pella). The combined thickness of the conductive tape and static-dissipative plastic is close to 0.5 mm, matching the thickness of the insulating mask—so that local airflow is not perturbed by thickness mismatch. Translation of the flat deposition target is performed by a robotic arm (Dobot Nova2) at 5 mm/s.

The spinning solution is 10 wt.% poly(ethylene oxide) (PEO, average Mv ~300,000, Sigma-Aldrich) in DI water. The solution is fed to the spinneret at 0.1 ml/h for electrospinning. The deposition time is 10 min.

For the deposition on a rod (Fig. 4C-E), the 12-mm-diameter rod is grounded and rotated at 400 rpm. The needle is biased at +15 kV. A 25 wt.% PEO blend is used at a 1 ml/h feed rate for faster deposition. The PEO blend is prepared by dissolving 3.5 wt.% high-molecular-weight PEO (average Mv ~2,000,000, Sigma-Aldrich) and 21.5 wt.% low-molecular-weight PEO (average Mv ~20,000, Sigma-Aldrich) in deionized water. To enable thicker fiber deposition, an active charge-neutralization module was integrated into the AFD setup. A discharging needle array, biased at −3 kV, is positioned on the opposite side of the guiding strip from the spinning needle, 5 mm from the grounded rotating bar. Corona discharge at the tips of the needle array generates negative ions to neutralize the positive charge accumulated on the rapidly depositing fiber layer. With the help of this discharging needle array, 1.2 mm of fiber is accumulated after 30 min of deposition. An airflow at 25 m/s, measured 1 cm from the nozzle outlet, is applied during deposition to align fibers.

2. AFD setup for melt blowing
Commercial polycaprolactone (PCL) filament (1.75 mm diameter; MSNJ) is fed into a 3D-printing pen (3D Pen PRO, MYNT3D) that serves as the spinneret. The hot-end temperature is set to 230 °C, and the PCL feed rate is measured to be 38.7 g/h. The extruded molten PCL is further drawn by hot air from a hot-air station (QUICK 861DE). The outlet of the 3D-printing

pen is positioned approximately 2 mm from a hot-air nozzle (NK2084, 8.4 mm diameter, QUICK). The hot-air station is operated at a set temperature of 450 °C and an airflow rate of 185 L/min. The spinning distance from the hot-air nozzle to the target is maintained at 120 cm. When the melt-blown PCL fibers reach the target, a room-temperature airflow parallel to the target surface is applied through the same 41-mm-wide nozzle (E-outstanding) to promote fiber deposition and alignment. The velocity of this cold airflow is 16 m/s at 1 cm from the airflow outlet. The total spinning time is 10 min.

3. Synthesis procedure for polymer-derived SiC fibers with AFD

The as-received AHPCS precursor (SMP-730, Starfire Systems) is first precured at 160 °C for 40 min in an oil bath. The oil bath consists of a glass beaker filled with mineral oil and heated on a hot plate with a temperature probe (PC-420D, Corning). The precursor is placed in a glass vial and immersed in the oil bath. Magnetic stir bars are placed in both the oil bath and the AHPCS vial, and both are stirred at 70 rpm during precuring. This step increases the viscosity of the precursor and prevents fiber merging after deposition.

After precuring, the polymer is dissolved in a binary mixture of toluene (anhydrous, 99.8%, Sigma-Aldrich) and N,N-dimethylformamide (anhydrous, DMF, 99.8%, Sigma-Aldrich) at a volume ratio of 7:3. The final polymer concentration is 65 wt.%. During dissolution, 0.1 wt.% benzophenone (99%, Sigma-Aldrich) is added as a photoinitiator for subsequent UV-induced crosslinking. The electrospun AFD process is identical to the setup of Fig. 4C–E, using the AHPCS solution at a 2 ml/h feed rate.

After deposition, the as-spun scaffold is first dried at room temperature for 12 h under reduced pressure from a building vacuum line (≈50 kPa) to remove residual solvent and stabilize the green structure, then UV-cured for 48 h under a 405 nm UV lamp (60 W, GIANTARM), which activates the benzophenone photoinitiator to crosslink the fibers. This step is critical for preserving fiber morphology and suppressing structural relaxation prior to pyrolysis.

The final step is pyrolysis. The crosslinked fiber scaffold is pyrolyzed into ceramic fibers in a furnace (WEBB 109, R.D. Webb Company Inc.) up to 1250 °C under vacuum (50 mTorr), with a temperature ramp rate of 1 °C/min and one-hour holds at 650 °C and 1250 °C. This thermal conversion removes organic constituents and transforms the crosslinked precursor into SiC, yielding a ceramic fiber scaffold suitable for subsequent composite fabrication. The β-SiC phase identification was performed using XRD (Malvern Panalytical Empyrean, Cu-Kα radiation, λ=0.154 nm).

References

1. Gay, D., *Composite materials: design and applications*. 2022: CRC press.
2. Hoa, S.V., *Principles of the manufacturing of composite materials*. 2009: DEStech Publications, Inc.
3. Elkington, M., et al., *Hand layup: understanding the manual process.* Advanced manufacturing: polymer & composites science, 2015. **1**(3): p. 138-151.
4. Parandoush, P. and D. Lin, *A review on additive manufacturing of polymer-fiber composites.* Composite Structures, 2017. **182**: p. 36-53.
5. Björnsson, A., *Automated layup and forming of prepreg laminates*. 2017, Linköping University Electronic Press.
6. Dirk, H.-J.L., C. Ward, and K.D. Potter, *The engineering aspects of automated prepreg layup: History, present and future.* Composites Part B: Engineering, 2012. **43**(3): p. 997-1009.
7. Pinchuk, L.S., *Melt Blowing: equipment, technology, and polymer fibrous materials*. 2002: Springer Science & Business Media.
8. Teo, W.E. and S. Ramakrishna, *A review on electrospinning design and nanofibre assemblies.* Nanotechnology, 2006. **17**(14): p. R89-R106.
9. Xu, C., et al., *Aligned biodegradable nanofibrous structure: a potential scaffold for blood vessel*

engineering. Biomaterials, 2004. **25**(5): p. 877-886.
10. Hobson, C.M., et al., *Fabrication of elastomeric scaffolds with curvilinear fibrous structures for heart valve leaflet engineering.* Journal of Biomedical Materials Research Part A, 2015. **103**(9): p. 3101-3106.
11. McClure, M., et al., *Electrospinning-aligned and random polydioxanone–polycaprolactone–silk fibroin-blended scaffolds: geometry for a vascular matrix.* Biomedical Materials, 2009. **4**(5): p. 055010.
12. Zhen, Q., et al., *Polypropylene-secondary alkane sulfonate micro/nanofibrous fabrics with aligned fibers for enhanced anisotropic wetting performances.* Applied Surface Science, 2022. **583**: p. 152486.
13. Li, D., Y. Wang, and Y. Xia, *Electrospinning of polymeric and ceramic nanofibers as uniaxially aligned arrays.* Nano letters, 2003. **3**(8): p. 1167-1171.
14. Li, D., Y. Wang, and Y. Xia, *Electrospinning nanofibers as uniaxially aligned arrays and layer-by-layer stacked films.* Advanced materials, 2004. **16**(4): p. 361-366.
15. Bazbouz, M.B. and G.K. Stylios, *Alignment and optimization of nylon 6 nanofibers by electrospinning.* Journal of Applied Polymer Science, 2008. **107**(5): p. 3023-3032.
16. Yarin, A.L., S. Koombhongse, and D.H. Reneker, *Bending instability in electrospinning of nanofibers.* Journal of applied physics, 2001. **89**(5): p. 3018-3026.
17. Xie, S. and Y. Zeng, *Turbulent air flow field and fiber whipping motion in the melt blowing process: experimental study.* Industrial & engineering chemistry research, 2012. **51**(14): p. 5346-5352.
18. Hekmati, A.H., et al., *Effect of needle length, electrospinning distance, and solution concentration on morphological properties of polyamide-6 electrospun nanowebs.* Textile Research Journal, 2013. **83**(14): p. 1452-1466.
19. Chang, H., et al., *Recreating the heart's helical structure-function relationship with focused rotary jet spinning.* Science, 2022. **377**(6602): p. 180-185.
20. Li, D., et al., *Collecting electrospun nanofibers with patterned electrodes.* Nano letters, 2005. **5**(5): p. 913-916.
21. Chaurey, V., et al., *Interplay of electrical forces for alignment of sub-100 nm electrospun nanofibers on insulator gap collectors.* Langmuir, 2010. **26**(24): p. 19022-19026.
22. Yan, Z. and J. Xie, *Electrically Guided Deposition of Electrospun Nanofibers for Fiber and Cell Pattern Formation.* Macromolecular Bioscience, 2025. **25**(9): p. e00151.
23. Bu, J., L. Chen, and J. Song, *In situ nanofibers patterned deposition based on electrostatic attraction–repulsion induction.* Chemical Engineering Journal, 2024. **480**: p. 147997.
24. Lavielle, N., et al., *Structuring and Molding of Electrospun Nanofibers: Effect of Electrical and Topographical Local Properties of Micro-Patterned Collectors.* Macromolecular Materials and Engineering, 2012. **297**(10): p. 958-968.
25. Kim, G.H., et al., *Electrospinning nanofiber on an insulating surface with a patterned functional electrolyte electrode.* Advanced Materials Interfaces, 2018. **5**(5): p. 1701204.
26. Chawla, K.K., *Composite materials: science and engineering*. 2012: Springer Science & Business Media.
27. Goren, A. and C. Atas, *Manufacturing of polymer matrix composites using vacuum assisted resin infusion molding.* Archives of materials Science and Engineering, 2008. **34**(2): p. 117-120.
28. Ichikawa, H., *Polymer-derived ceramic fibers.* Annual Review of Materials Research, 2016. **46**: p. 335-356.
29. Frank, E., F. Hermanutz, and M.R. Buchmeiser, *Carbon fibers: precursors, manufacturing, and properties.* Macromolecular materials and engineering, 2012. **297**(6): p. 493-501.

Supplemental Materials

Aerodynamic fiber deposition: additive manufacturing continuous fiber reinforcement with patternable alignment

Luochang Wang, Simeng Wu, Paulson Varghese, Jung-Kun Lee, Qihan Liu

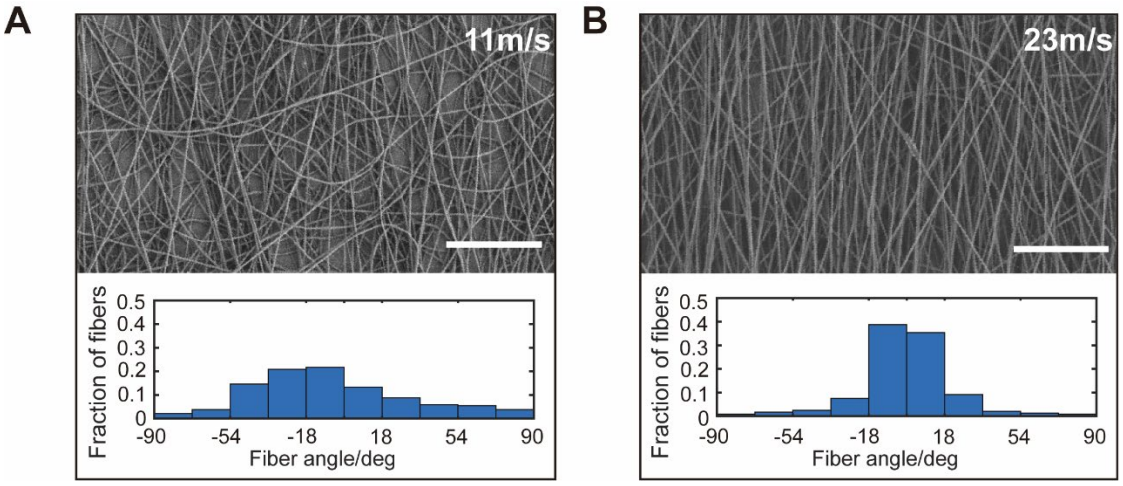

Figure S1. How airflow aligns fibers. (A) Fiber deposits with poor alignment under an airflow below 20 m/s. **(B)** Fiber deposits with good alignment under an airflow above 20 m/s. In each panel, the spinning was carried out for 10 minutes, and the downstream region right after the blank region was selected as the position for imaging. The scale bars are 10 μm.

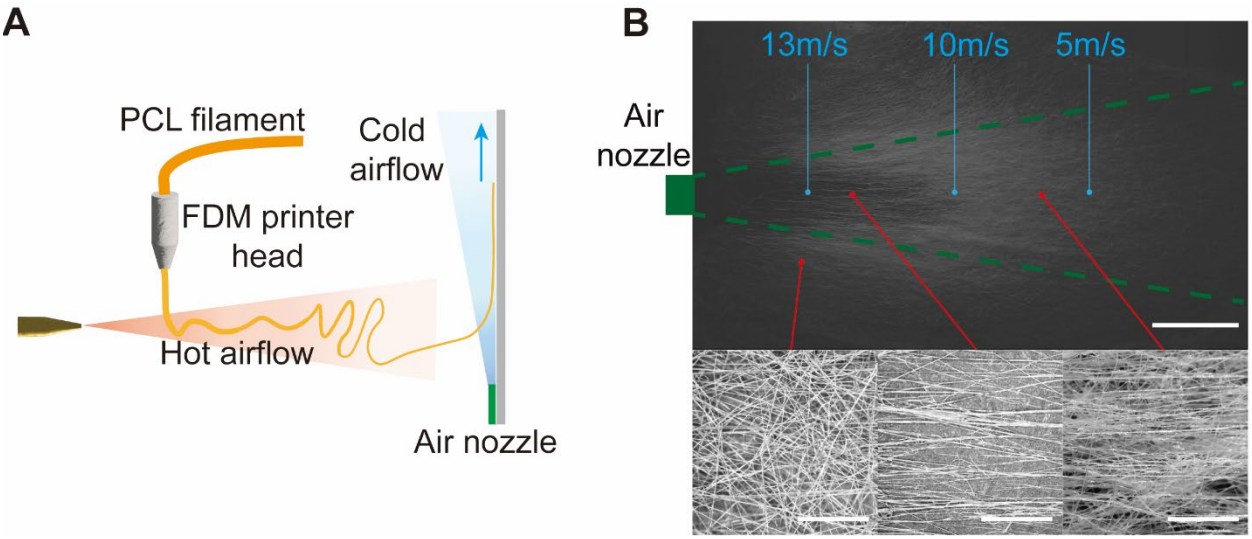

Figure S2. AFD applied to melt blowing. (A) A simple melt blowing setup was constructed by extruding molten polycaprolactone (PCL) from the hot end of a 3D printing pen. **(B)** Photo of the deposition produced by melt-blown AFD shows that the deposition region elongates along the v_{air} direction. The top photo has a scale bar of 10 cm. The bottom row shows optical microscope images of the fibers from different locations with scale bars of 5 mm.

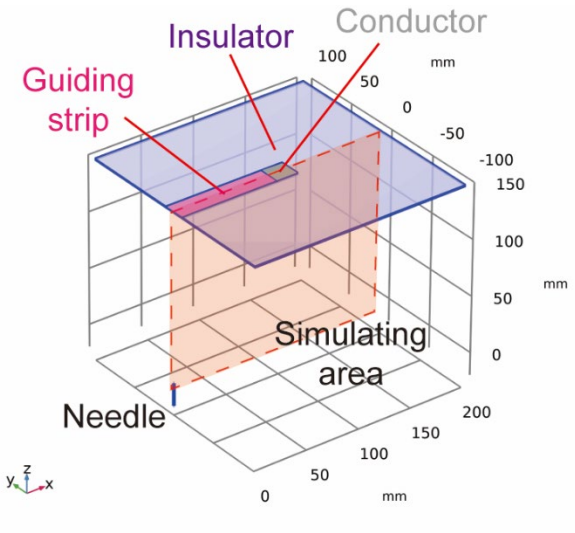

Figure S3. Simulating the electric field. The simulation is performed in COMSOL Multiphysics 6.2. The conductivity of the air is assumed to follow a power-law relation $\sigma_{fiber} = \sigma_{ref}\left(E/E_{ref}\right)^{m}$. Here E is the local electric-field magnitude, $E_{ref} = \Delta V/L = 10^5$ V/m is the nominal applied field, where $\Delta V = 15$ kV is the spinning voltage and $L = 15$ cm is the needle-target distance. m = 0, 1, and 2 correspond to constant, linear, and quadratic field-dependent conductivity, respectively. The reference conductivity σ_{ref} is estimated from the typical electrospinning current $I \sim 1$ μA and the deposition area of $A \sim 1$ cm^2, which gives $\sigma_{ref} \sim IL/(A\Delta V) \sim 10^{-7}$ S/m. The insulating mask, the side of the needle, and the wall of the simulation domain are all modeled with the no-current boundary condition. The conductor surface and the needle tip are modeled with constant electric potential. The orange area going through the center of the guiding strip, deposition window, and the needle is used to visualize the electric field in Fig. 3 and subsequent figures.

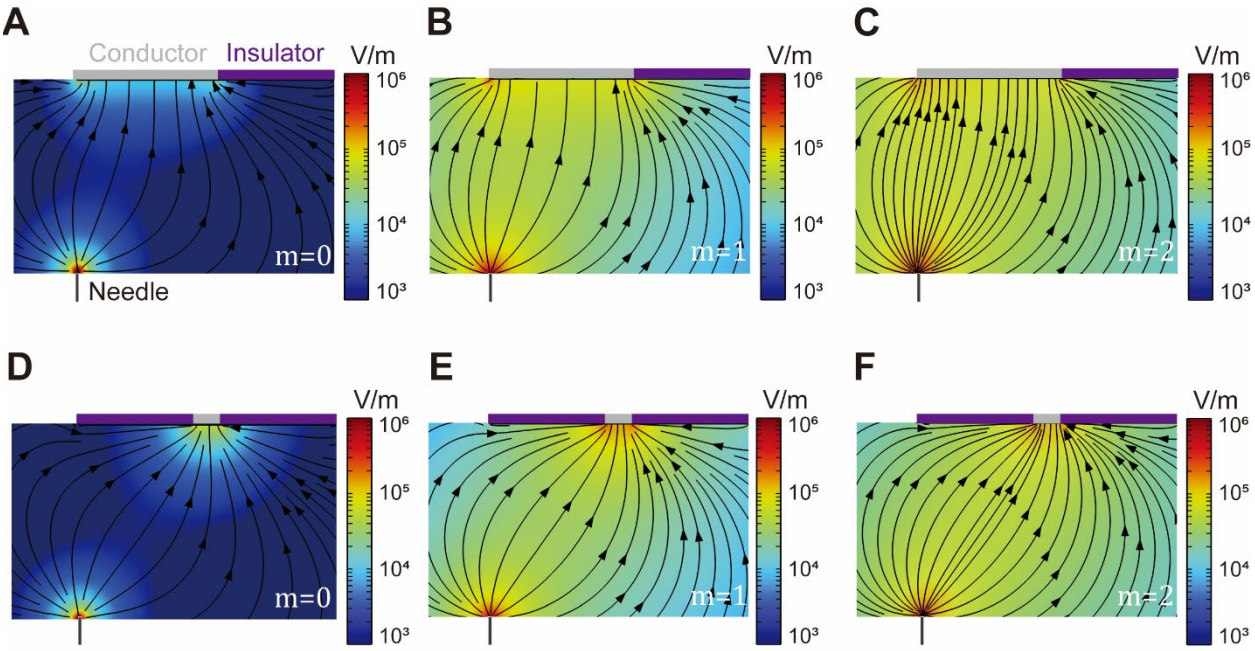

Figure S4. The effect of field-dependent conductivity. The power-law exponent m does not affect the qualitative effect of reducing the size of the deposition window. The conclusion that reducing the window size increases the local electric field, thus reducing fiber alignment, is valid regardless of the specific m used in the simulation.

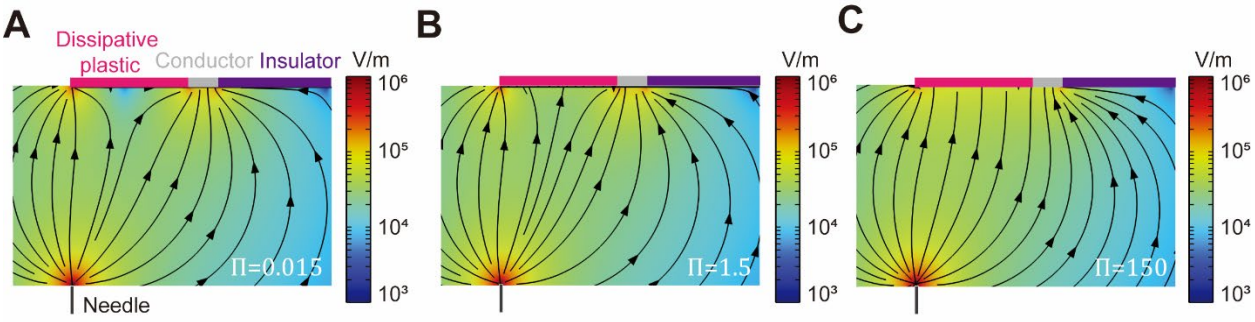

Figure S5. The effect of guiding strip conductance. The effect of guiding strip conductance is studied using the dimensionless ratio: $\Pi = g_p / g_{ref} = \frac{\sigma_p/t_p}{\sigma_{ref}/L}$. Here g_p is the through-thickness areal conductance of the dissipative plastic, g_{ref} is the reference areal conductance across the air gap. $t_p = 1$ mm is the thickness of the dissipative plastic. **(A)** For a low-conductance guiding strip with $\Pi = 0.015$, the electric field is similar to the insulator case. **(B)** If the conductance of the air and strip are comparable ($\Pi = 1.5$), the electric field is noticeably altered by the conductance of the strip. **(C)** For a highly conductive guiding strip, the electric field becomes identical to the case of an exposed conductive target.